

Geophysical Research Letters

RESEARCH LETTER

10.1029/2021GL093309

Key Points:

- A *SV*-wave velocity model near the southernmost Mariana Trench is derived
- The incoming Pacific Plate is characterized by low velocities (3.6–4.1 km/s) within the upper mantle near the southern Mariana Trench
- Velocity reduction/hydration in the forearc mantle is not as large as in central Mariana

Supporting Information:

Supporting Information may be found in the online version of this article.

Correspondence to:

H. Yang,
hyang@cuhk.edu.hk






Citation:

Zhu, G., Wiens, D. A., Yang, H., Lin, J., Xu, M., & You, Q. (2021). Upper mantle hydration indicated by decreased shear velocity near the southern Mariana Trench from Rayleigh wave tomography. *Geophysical Research Letters*, 48, e2021GL093309. <https://doi.org/10.1029/2021GL093309>

Received 16 MAR 2021

Accepted 20 JUL 2021

Upper Mantle Hydration Indicated by Decreased Shear Velocity Near the Southern Mariana Trench From Rayleigh Wave Tomography

Gaohua Zhu¹ , Douglas A. Wiens² , Hongfeng Yang¹ , Jian Lin^{3,4,5} , Min Xu^{3,6} , and Qingyu You⁷

¹Faculty of Science, Earth System Science Programme, The Chinese University of Hong Kong, Hong Kong, China, ²Department of Earth and Planetary Sciences, Washington University in St Louis, St Louis, MO, USA, ³Key Laboratory of Ocean and Marginal Sea Geology, South China Sea Institute of Oceanology, Innovation Academy of South China Sea Ecology and Environmental Engineering, Chinese Academy of Sciences, Guangzhou, China, ⁴Department of Ocean Science and Engineering, Southern University of Science and Technology, Shenzhen, China, ⁵Department of Geology and Geophysics, Woods Hole Oceanographic Institution, Falmouth, MA, USA, ⁶Southern Marine Science and Engineering Guangdong Laboratory (Guangzhou), China, ⁷Key Laboratory of Petroleum Resources Research, Institute of Geology and Geophysics, Chinese Academy of Sciences, Beijing, China

Abstract Reduction of seismic velocities has been employed to study the hydration of incoming plates and forearc mantle in recent years. However, few constraints have been obtained in the Southern Mariana Trench. We use an ocean bottom seismograph (OBS) deployment to conduct Rayleigh wave tomographic studies to derive the *SV*-wave velocity structure near the Southern Mariana Trench. Measured group and phase velocities as a function of period are inverted to determine the *SV*-wave velocity using a Bayesian Monte Carlo algorithm. The incoming Pacific Plate is characterized by low velocities (3.6–4.1 km/s) within the upper ~25 km of the mantle near the trench, indicating extensive mantle hydration of the incoming plate in southern Mariana. The velocity reduction in the forearc mantle is not as large as in central Mariana, most likely indicating a lower forearc serpentinization in this region, which is consistent with the absence of serpentinite mud volcanoes.

Plain Language Summary Estimating the amount of water carried by the subduction zone into Earth's interior plays an important role in the global water cycle, but is poorly constrained at subduction zones due to the lack of near-field observations. We utilize data recorded by OBSs near the Southern Mariana Trench. Using seismic imaging methods, we construct an *SV*-wave velocity model beneath the southernmost Mariana subduction zone. Our model demonstrates low-velocity anomalies within the upper ~25 km mantle near the trench, suggesting a large amount of water input in southern Mariana. Furthermore, our seismic observations suggest that low degree serpentinization of the forearc mantle in southern Mariana than central Mariana, agree with the lacking of serpentinite mud volcanoes in the forearc.

1. Introduction

The properties of incoming oceanic plates, such as their geometry and water content closely influence various processes in subduction zones, including the generation of earthquakes and arc magmatism (Grove et al., 2009; Shillington et al., 2015). Water content is especially important because water transported by the incoming plate cools the subduction zone, promotes forearc metamorphism, and facilitates the generation of arc magmatism (Fujie et al., 2016; Hyndman & Peacock, 2003). Since the subducting slab is the primary channel through which water can enter the Earth's interior, estimating hydration of the incoming plate at subduction zones is important for studying these processes (Hirschmann, 2006; Van Keken et al., 2011). Especially at the trench-outer rise bending region on the incoming plate, substantial normal faults can extend into the uppermost mantle, and thus water can penetrate through the bending faults into the mantle, leading to a pervasively serpentinized region (Ranero et al., 2003).

Seismic imaging significantly contributes to constraining the hydration of subduction zones, since mineral hydration leads to a reduction in seismic velocity (Cai et al., 2018; Shillington et al., 2015; Tibi et al., 2008).

Various properties of the subducting oceanic plate may affect the hydration of the incoming plate, such as plate age, thermal structure, and structural changes caused by bending faults (Fujie et al., 2018; Van Keken et al., 2011). Therefore, the estimated hydration of incoming plates varies between global subduction zones, even between different segments of the same subduction zone. For example, the abrupt changes in plate hydration between the Shumagin Gap and the Semidi segment in the Alaska Peninsula are attributed to different orientations and styles of the pre-existing structures in the subducting plate (Shillington et al., 2015). In the Japan Trench, along-trench variations in the seismic structure are obvious and a high hydration zone is closely related to pervasive fracturing of the ancient fracture zone on the oceanic plate (Fujie et al., 2016). Differences in plate hydration between the Japan and Kuril Trenches are also closely related to the spatial variation of the bending faults, which is caused by diverse angles between the current trench and fossil ridge (Fujie et al., 2018).

The Mariana Subduction Zone (MSZ) is regarded as a water-rich system based on the observation of active serpentine mud volcanoes (Fryer et al., 1999) (Figure 1a) and low upper-mantle velocities (Cai et al., 2018) in central Mariana. Due to either increasing curvature of the Mariana system with time or oblique convergence toward the south, the geological setting and physical processes of southern Mariana are different from those in central Mariana (Stern et al., 2003). For example, a shorter Wadati-Benioff zone (Zhu et al., 2019), the diffuse deformation of the upper plate (Martinez et al., 2018), and an incipient island arc (Ribeiro et al., 2020) have been reported in southern Mariana. However, we have limited knowledge about how the hydration of the incoming plate and the forearc mantle varies between different segments of the MSZ due to the absence of observations. In southern Mariana, a previous study derived a *P*-wave velocity model of the crust and uppermost mantle structure using active-source OBS data (Wan et al., 2019) (Figure 1d). The subducting plate has an average crustal thickness of ~ 6.0 km with V_p of 7.0 ± 0.2 km/s at the base of the crust and 7.0–7.3 km/s in the uppermost mantle, while the overriding plate has a maximum crustal thickness of ~ 18 km beneath the forearc with V_p of ~ 7.4 km/s at the crustal bottom and 7.5–7.8 km/s in the uppermost mantle. The velocity reduction in the uppermost mantle of both subducting and overriding plates is interpreted as mantle serpentinization. However, the distribution of serpentinized mantle in southernmost Mariana is still unclear.

In this study, we therefore aim to derive the *SV*-wave velocities in southern Mariana using a near-field passive ocean-bottom seismographs (OBS) data set and compare with the results obtained in central Mariana, which could help investigate the distribution of serpentinized mantle in southernmost Mariana and potential along-trench variations in incoming plate hydration in the MSZ. The study utilizes seismic records collected by 12 OBSs in the Southern MSZ between March and June 2017 (Zhu et al., 2020). The deployment covers the forearc and incoming plate region (Figure 1b). We derived local Rayleigh-wave group and phase velocity dispersion curves using ambient noise and Eikonal tomography methods. A Bayesian Monte Carlo algorithm was then used to determine the shear-wave velocity of the crust and uppermost mantle. Due to the limited array size and azimuth coverage, we only derived a 2-D image of the azimuthally averaged velocity model of the vertically polarized *S* waves (*SV*-waves).

2. Geologic Setting

The Mariana system differs from other convergent margins in that where the cold, old Mesozoic Pacific Plate (~ 140 – 150 Ma) is subducted beneath the Philippine Sea Plate (Figure 1a) started at ~ 52 Ma (Arculus et al., 2015). South of 13.8°N , the southernmost Mariana arc-trench system trends nearly E-W in comparison to the N-S orientation of most of the Mariana arc-trench system to the north. The volcanic arc is well defined north of the Guam Island, whereas a well-developed volcanic arc does not exist southwest of the Tracey Seamount (Figure 1b). Instead, the southern Mariana arc is composed of small volcanic edifices that are irregularly spaced (Ribeiro et al., 2020). The Alphabet Seamount Volcanic Province (ASVP, an unusual cluster of small basaltic volcanoes) vents are located about 50–70 km southwest of the Tracey Seamount, with no sign of concentrated magmatic activity around a single vent, suggesting where the next major Mariana arc edifice should be (Stern et al., 2013; Ribeiro et al., 2020).

Along the Mariana forearc southwest of Guam, the Mariana forearc is divided into northeastern and active southern parts by the West Santa Rosa Bank Fault (WSRBF) tectonic boundary located at $\sim 144^\circ\text{E}$, separating

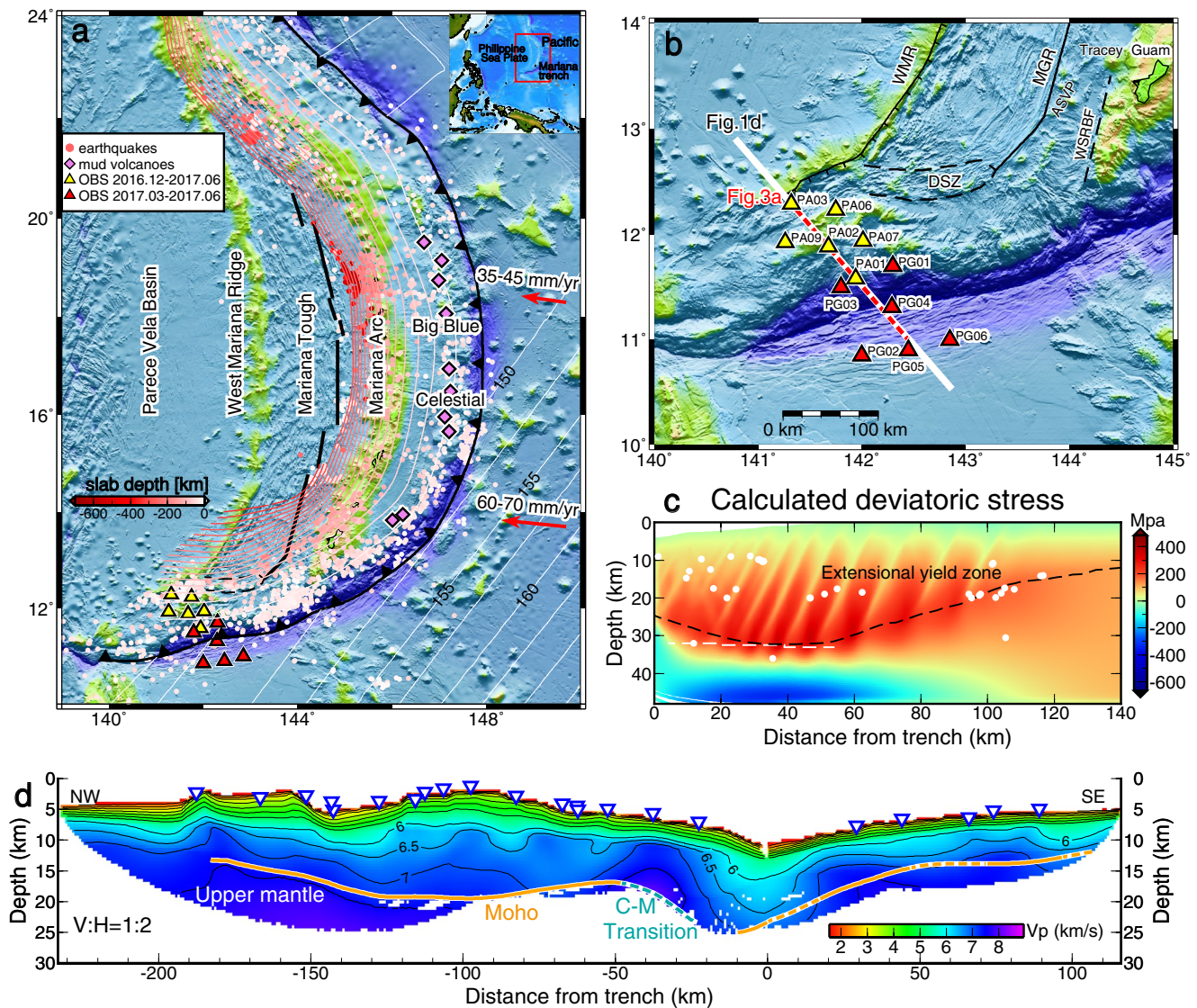


Figure 1. (a) Topographic map of the Mariana Trench. White lines show crustal age (Ma) contours of the Pacific Plate. The colored curves within the overriding plate represent the subducted slab depth based on the Slab 2.0 model (Hayes et al., 2018). Red arrows show the convergence direction of the Pacific plate relative to the forearc (Kato et al., 2003). (b) The map of OBS locations (red and yellow triangles represent two OBS deployments: 2017.03–2017.06, 2016.12–2017.06, respectively) in southern Mariana. The thick white line and the red dashed line show the profile of the V_p model in Figure 1d and the V_s model in Figure 3a, respectively. WMR: West Mariana Ridge; MGR: Malaguana-Gadao Ridges; DSZ: Diffuse spreading zone; WSRBF: W. Santa Rosa Bank transform fault; ASVP: Alphabet Seamount Volcanic Province. (c) Comparison of the calculated deviatoric stress with the velocity model and distribution of outer-rise seismicity. The calculated deviatoric stress in southern Mariana is from Zhou and Lin (2018). The black dashed curve is the calculated boundary between the extensional yield zone and the elastic core. The white dashed line represents the V_s -wave velocity contour of 4.1 km/s. The white dots show the outer-rise seismicity within ± 30 km from the profile relocated using the ocean-bottom seismographs (OBS) data (Zhu et al., 2019). (d) The V_p model from Wan et al. (2019) based on active-source OBS experiments. Brown solid and dash lines indicate the Moho depths relatively well constrained by PmP arrivals and the estimated Moho depths without good PmP constraints, respectively. The green dashed line (C-M Transition) stands for the lower boundary of a hypothesized crust-mantle transition.

two tectonic provinces of very different physiognomies and tectonic evolution history (Fryer, 1996; Ohara et al., 2012). In contrast to the broad forearc to the northeast, the southernmost Mariana forearc is deforming rapidly, which is cut by numerous normal and strike-slip faults striking parallel and perpendicular to the trench axis, suggesting strong along-strike and trench-perpendicular extension in this region (Martinez et al., 2018). Although a number of serpentinite mud volcanoes (e.g., Big blue and Celestial seamounts; Figure 1a) exist in the northern Mariana forearc ~ 30 – 120 km behind the trench axis (Fryer et al., 1999), none is known to exist along the southern Mariana forearc except that serpentinitized peridotites are sampled on

the inner trench slope along the southern Mariana forearc (Ohara et al., 2012; Okumura et al., 2016). The region has rapidly evolved and reorganized to accommodate the opening of the southern tip of the Mariana Trough (Martinez et al., 2018; Ribeiro et al., 2020).

3. Data and Methods

The data analyzed in this study were collected during two OBS experiments conducted in the southern MSZ, including a total of 12 OBSs equipped with a three-component sensor and a hydrophone. The OBS (STS-G60) was developed by Institute of Geology and Geophysics, Chinese Academy of Sciences. The OBS sensor had a designed lower frequency response of 30 s, allowing a sample rate of 100 Hz. During the first OBS deployment of the “Challenger Deep” expeditions in December 2016, seven OBSs were deployed in the fore-arc region, and six of them were successfully recovered in June 2017 (the PA* OBS stations shown in Figure 1b). The other six OBS stations (the PG* OBS stations shown in Figure 1b) were deployed in March 2017 and recovered at the same time as PA* OBSs, which mostly cover the region of the incoming plate on the outer trench slope.

We conducted ambient noise tomography (ANT) similarly to previous studies (Bensen et al., 2007; Lin et al., 2008, 2009). The daily vertical-component seismograms were bandpass filtered at 80–0.2 s period after removal of the mean and trend. Spectral whitening was applied to minimize the effects of large earthquakes and the data were then down-sampled to 10 samples per second to speed up the calculation. Seismograms from all OBS pairs were then cross-correlated and stacked over the entire deployment period to derive empirical Green functions between OBS pairs, from which the Rayleigh waves can be identified up to the period of ~17 s (Figure S1). We then measured the Rayleigh-wave group and phase speeds as a function of the period using the frequency-time analysis (FTAN) (Figure S2) (Levshin & Ritzwoller, 2001; Ritzwoller & Levshin, 1998). To construct a reference V_s model for extracting the most reasonable phase velocity dispersion curve, we combined the crustal P -wave velocity structure divided by a V_p/V_s ratio of 1.8 (Wan et al., 2019; Zhu et al., 2019) with the IASP91 model in the deeper part (Kennett & Engdahl, 1991). Due to the effect of the water layer on the Rayleigh-wave phase and group velocities, we also combined the solid reference model with a water layer of the average water depth between an OBS pair. All dispersion curves were manually examined to discard those with physically unreasonable values and inconsistent measurements at adjacent periods. Eventually, 42 dispersion curves were used for the phase-velocity inversion. For each frequency, only station pairs with distances larger than one and half of the wavelength and signal-to-noise ratio (SNR) >3 were kept. We then produced Rayleigh group- and phase-velocity maps between 6 and 17 s on a grid of node spacing of $0.3 \times 0.3^\circ$ using the ray-theory-based tomographic method (Figure S3) (Barmin et al., 2001). Due to the insufficient station coverage in our study region, we only solved for the isotropic component of the Rayleigh-wave group and phase velocity and did not consider the anisotropic components during tomographic inversion.

Similar to the procedures described in Jin and Gaherty (2015), we applied the Eikonal tomography (ET) method to teleseismic Rayleigh waveforms to determine phase velocities at longer periods. We selected earthquakes with surface-wave magnitudes >5 and epicentral distances between 18° and 150° based on the USGS catalog. To discard noisy seismograms, we chose 45 earthquakes with an SNR for surface waves >2 on at least four OBSs (Figure S4). Most of them were distributed at Bougainville trench, Philippine trench, Ryukyu trench and Alaska trench. For each earthquake and each period, the phase delays were calculated by cross-correlating the narrow-band filtered seismogram on the vertical component from a given station with the seismograms from all other nearby stations (Jin & Gaherty, 2015). To further eliminate the influence of poor-quality seismograms, the coherence between waveforms from nearby stations was estimated, and only those measurements with coherence >0.5 were included. We then inverted the phase delays to produce apparent phase velocity maps with a spacing of 0.3° between periods of 21 and 36 s (Figure S3).

The ANT and ET results were combined to obtain more complete measurements of phase velocity dispersion curves. Due to the limited data quality at the interested periods, our ANT and ET results do not overlap at any period, making the comparison of measurements from the two methods impossible. We constructed the finalized phase speed dispersion curves by directly combining the ambient noise and earthquake measurements. A three-point running average was then applied to smooth the dispersion curve. Group velocity

results from ANT (6–17 s) were also included for the SV-wave velocity inversion to better fit water depth and to improve resolution for shallower structure. The uncertainties of phase velocities were inferred by adopting the empirical scaling relationship between resolution in structure (in km) and uncertainty in velocity (in m/s) (Feng & Ritzwoller, 2019; Shen et al. 2016). In our study, we used the k value of $\sim 0.8 \times 10^{-3} \text{ s}^{-1}$, so that a 50-km resolution produces an uncertainty estimate of ~ 40 m/s. Uncertainties of group velocities were computed by multiplying the uncertainties of phase velocities by a factor of 2.0 (Shen et al. 2016). For phase velocities from ET (21–36 s), the uncertainties were normalized at each period based on the standard deviation of phase velocities. Considering the limited OBS array size, we took the weighted mean of dispersion curves at neighboring nodes with similar distances from the trench, and applied the Bayesian Monte Carlo inversion to obtain a 1-D shear-velocity structure. Then the V_s results were projected along a 1-D transect to get the 2-D V_s structure across the trench.

The Bayesian Monte Carlo algorithm was used to invert the azimuthally averaged SV-wave velocity (Shen et al., 2013, 2016; Shen & Ritzwoller, 2016). To impose prior constraints on water depth, crustal velocity and thickness and other parameters, we constructed the SV-wave velocity model at each node, with perturbations relative to the initial model and model constraints. Each model consisted of three layers on top of a half-space: (a) a water layer starting from the average depth within the region of 0.5° surrounding the node and with an allowed perturbation of ± 1.0 km; (b) crust; and (c) upper mantle from the Moho to a depth of 120 km. For the crustal layer, we adopted different model parameters between the incoming and overriding plates. For the incoming plate, the crustal thickness started around the value of 7 km with a perturbation of ± 2 km. The crustal velocity was assumed to increase linearly with depth from $V_{sv} = 2.3$ km/s at the top to $V_{sv} = 3.5$ km/s at the bottom of the layer with $\pm 25\%$ perturbations. For the overriding plate, we used a starting value of 14 km based on the previous active-source seismic survey in the study region and allowed a perturbation of ± 2.5 km for the crustal thickness. The crustal V_{sv} was parameterized by four B-spline coefficients with $\pm 25\%$ perturbations. The upper-mantle V_{sv} was parameterized by a B-spline, which was defined by six nodes with a $\pm 25\%$ perturbations. We also imposed the constraints that velocity contrast across the Moho discontinuity was positive and V_{sv} increased monotonically with depth in the crust. For a single grid node, the best fitting model was determined and models were accepted if their χ^2 misfit was smaller than 50% higher than that of the best fitting model (Shen et al., 2013, 2016). Models with mantle velocity higher than 4.9 km/s were excluded. An average model was finally calculated from all accepted models. Examples of the SV-wave velocity inversion at four representative nodes are shown in Figure 2. The results of the Bayesian Monte Carlo inversion fit the measured group- and phase-velocity dispersion curves well. The inverted SV-wave velocities at each node were projected on the 2-D profile across the trench.

4. Results

The azimuthally averaged velocity model of vertically polarized S waves (V_{sv}) clearly shows obvious velocity reduction in the upper mantle (Figures 3a and 3b). Here, we adopted the assumption that the shear-wave velocity of 4.1 km/s is a conservative value for estimating the serpentinized mantle, considering that water-filled cracks can also lower seismic velocity (Cai et al., 2018). Therefore, the value of 4.1 km/s was used to define the low-velocity zone (LVZ) despite the lack of an obvious boundary. To verify the robustness of the velocity model, we conducted synthetic tests with two additional models, one with a gradual velocity change in the upper mantle (Model 1) and the other one having a LVZ with sharp boundaries (Model 2). Using the same inversion parameters, we can successfully recover the two models (see Supplementary text). The 1-D velocity profiles in our final model are close to the synthetic Model 1 with gradual velocity change (Figures S6b and S6d). The absence of a sharp boundary may reflect gradually changed velocities due to decreased serpentinization with depth or smooth effects of inversion on the depth range of a low-velocity layer.

Beneath the incoming plate near the trench, the upper mantle is characterized by slow velocities at depths shallower than 32 km, with velocities as low as 3.6 km/s. The low-velocity zone reaches 32 ± 7 km beneath the seafloor, which is 25 ± 7 km beneath the Moho. Note that the depth and thickness uncertainties quoted here and elsewhere were estimated based on variations in thickness obtained by perturbing the assumed velocity bounding the serpentine layer by ± 0.1 km/s. The crustal thickness of the incoming Pacific Plate is

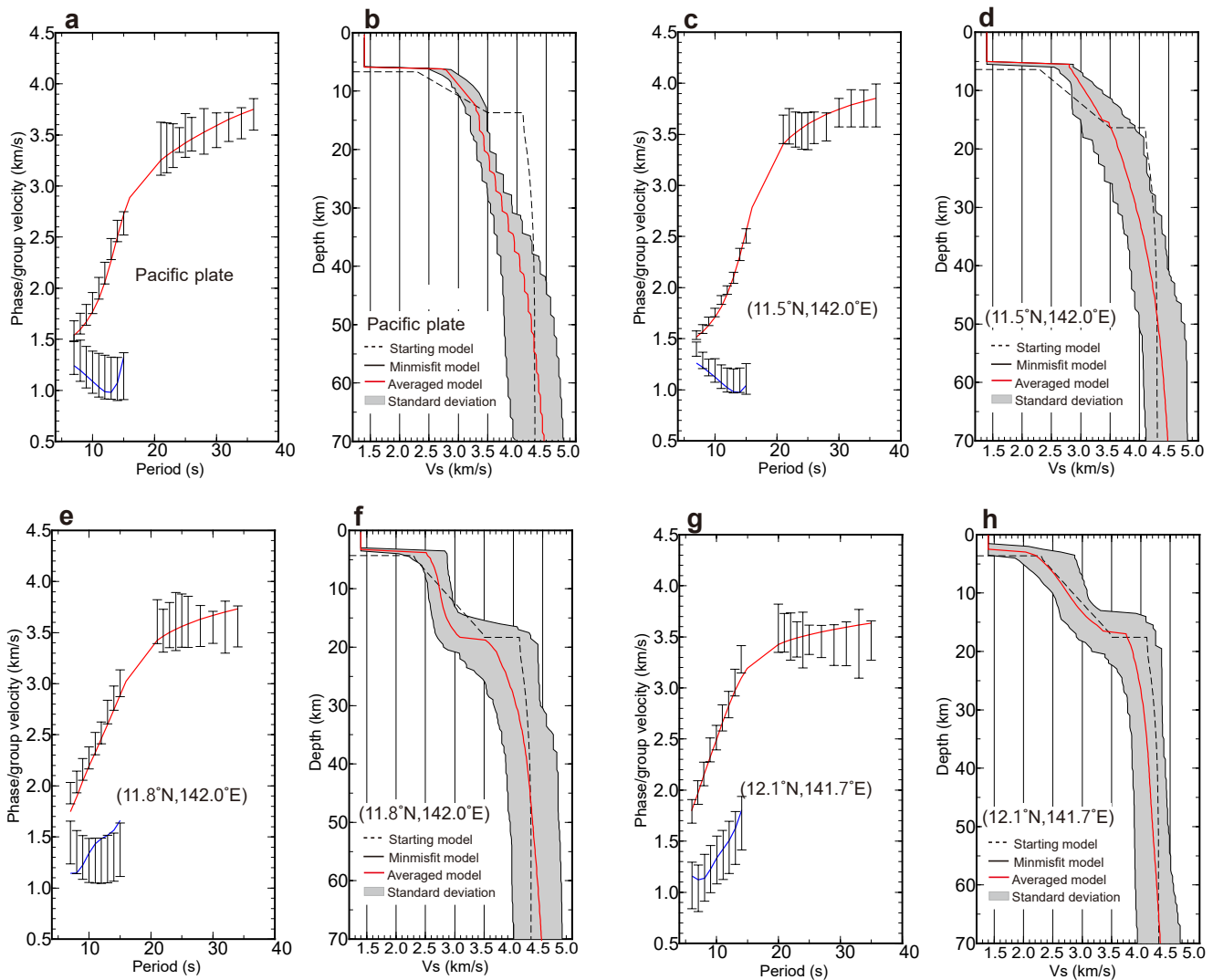


Figure 2. Bayesian Monte Carlo inversion at example nodes. (a) The combined phase velocity measurements from the ambient noise tomography and Eikonal tomography (black error bars) and predicted phase (red line) and group (blue line) dispersion curves from the averaged model of Bayesian Monte Carlo inversion. (b) Shear-velocity model from the Bayesian Monte Carlo inversion. The red solid curve represents the average model and the black dashed curve is the starting model. Notions in (c), (e), and (g) are the same as in (a); notions in (d), (f), and (h) are the same as in (b).

~7.0 km, and is largely fixed by the prior constraints from the *P*-wave velocity model derived from the active source data (Wan et al., 2019).

The normal faults in 2-D bending analyses are estimated to penetrate to 32 km below the seafloor in southern Mariana, which were constrained by the observed flexural deformation and normal faulting (Zhou & Lin, 2018). Interestingly, the depth of velocity contour of 4.1 km/s bounding the serpentinization depth matches well with the estimated maximum depth of normal faulting predicted by the deviatoric stress model (Figure 1c). Furthermore, the velocity reduction of the forearc mantle is also observed in the *SV*-wave velocity model of the study region, but it is not as large as the forearc mantle in central Mariana (Cai et al., 2018) in the depth ranges of 15–30 km beneath the seafloor (Figure 3c). Based on our synthetic tests, we infer that the velocity reduction in the forearc mantle in southern Mariana is smaller than that in central Mariana.

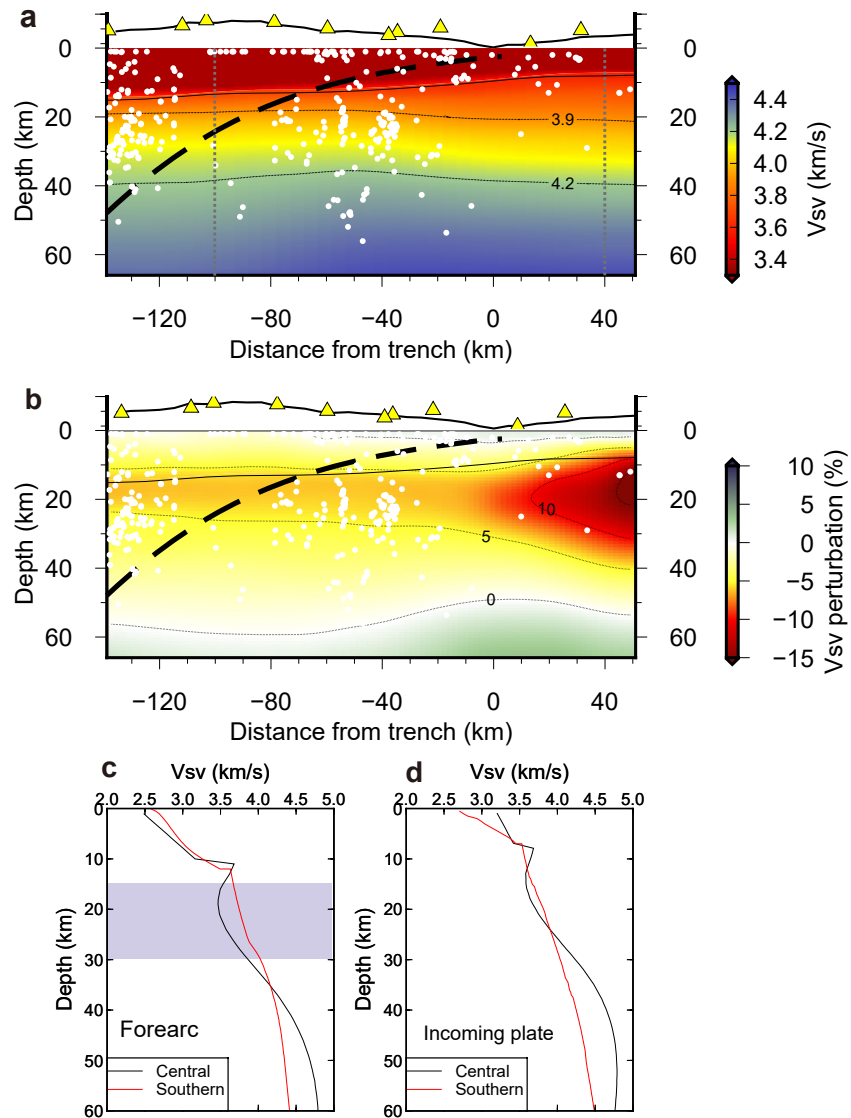


Figure 3. Velocity profile in southern Mariana. (a) The vertical profile showing the azimuthally averaged velocity of vertically polarized S waves (V_{sv}) along the red dashed line in Figure 1b. The black dashed lines are velocity contours of labeled values. White dots are relocated earthquakes around the profile from a previous study (Zhu et al., 2019). The thick dashed black line shows the location of the slab from the Slab 2.0 model (Hayes et al., 2018). The solid black line marks the Moho from the inversion. Two vertical dashed gray lines mark the locations of the 1-D V_{sv} structure shown in Figures 3c and 3d. (b) Velocity perturbation relative to the initial model. (c)-(d) Comparison of the V_{sv} structure between central Mariana (Cai et al., 2018) and southern Mariana in the forearc (c) and incoming plate region (d), respectively. The velocity reduction of the forearc upper mantle is not as large as that in central Mariana as highlighted by the light purple shadow in (c).

5. Discussion

Tectonic activities in southern Mariana convergent margin reflect the unique setting and provide important perspectives on the structure and evolution of convergent margins. In this section, we discuss three new insights that the newly obtained seismic constraints have provided: (a) the serpentinization degree and water content of the incoming plate indicated by the low velocities of the upper mantle; (b) how the low-velocity zone of the incoming plate correlated with the predicted extensional yield zone and the distribution of incoming plate seismicity; (c) how the unusual tectonics of southern Mariana have affected the development of the forearc mantle serpentinization and a normal magmatic arc.

5.1. Implication for Water Input

The seismic image of the southern Mariana region shows a low-velocity zone at the top of the incoming plate mantle (Figure 3a), which is likely related to the hydration of mantle peridotite to form serpentine minerals as well as free water in the fault zones. The estimates of hydration degree and extent could provide constraints on the amount of water carried into the southern MSZ. To estimate the water content due to serpentinization of the subducting slab, we made the assumptions similar to Cai et al. (2018), that the low-velocity zone corresponds to the shear-wave velocities of 4.1 km/s and the additional velocity reduction (~ 0.3 km/s) within the low-velocity zone in the slab before subduction is attributed to pore water in cracks. Noted that serpentinization may occur at depths greater than this velocity contour, but the 4.1 km/s gives a conservative estimate. Estimating the water content also requires the relationship between the seismic properties and the degree of serpentinization. Lizardite, the low-temperature form of serpentine, is expected to predominate at depths shallower than 30 km beneath the seafloor based on the colder temperatures (roughly 470°C). The assumption that the velocity reduction is due to lizardite yields smaller serpentinization estimates compared to antigorite, so it provides an estimate of the lower bound of water input (Cai et al., 2018; Ji et al., 2013).

Based on the experimental relationship between seismic velocities and serpentinization degree (Ji et al., 2013) ($V_s = 4.51 - 2.19 \times \Phi$, where Φ is the serpentine volume fraction), shear wave velocities of 3.6–4.1 km/s are likely related to the serpentinization of ~ 19 –41 vol% (i.e., ~ 1.9 –4.3 wt%). We therefore interpret the seismic images as the evidence for a 25-km-thick, partially serpentinized (~ 1.9 –4.3 wt% water) slab-mantle zone near the trench. The estimates are consistent with the observed V_p values of 7.0–7.5 km/s that indicate 32–38 vol% of serpentinization within the uppermost mantle (Wan et al., 2019). Our interpretation of serpentinization extending to depths of ~ 32 km below the seafloor in the incoming plate indicates great hydration (water content) of the incoming plate at the southern Mariana.

The low velocities (3.6–4.1 km/s) within the upper mantle of the incoming plate are observed at both the southern and central Mariana (Figure 3c). Considering the uncertainties of both studies, the estimated hydration depth of the incoming plate mantle is nearly identical between the central Mariana (Cai et al., 2018) and the southern Mariana. Due to the limited resolution at depths greater than 50 km in our velocity model (Figure S5) and the smoothing effects of inversion on the low-velocity zone over a wider depth range (Figure S6), we prefer not to further explain any differences at greater depths. Note that the Earth may have an even slower velocity and a higher rate of serpentinization than what is suggested in the current image. Indeed, the results of the synthetic tests (Figure S6) show that a sharp velocity reduction is not fully recovered in the current data set and model parameterization. As such, the current result provides a conservative estimation of serpentinization in this region and only reveals the first-order velocity variations across the trench, and a better assessment and the along-strike variations should be subject to future investigation with more data.

5.2. Coherence Between Low-Velocity Zone (Hydration Zone) and Bending Faulting

Normal faults arising from the plate bending provide pathways for water to penetrate deep into and hydrate the subducting slab, despite that the uppermost mantle is assumed to be largely anhydrous due to the extraction of water by melting at the mid-ocean ridge (Hirth & Kohlstedt, 1996). The occurrence of incoming plate normal-faulting earthquakes is an indication that bending stresses could exceed the rock yield strength, causing permanent deformation and extensional faulting earthquakes in the upper plate (Zhang et al., 2014, 2018; Zhou et al., 2015). These plate-bending earthquakes occur along faults that facilitate the hydration of the subducting plate, therefore we may infer the hydration extent based on the lateral and depth distribution of normal faulting earthquakes (bending faulting). For example, previous studies suggested the neutral plane with a global average depth of 30–40 km marks the bottom boundary of the mantle hydration, assuming that pore water cannot penetrate the compressional stress regime (Chapple & Forsyth, 1979). Based on near-field OBS observations, the extensional earthquakes are estimated at the depth of ~ 20 km below the Moho in the central Mariana, which is much deeper than previous results (Emry et al., 2014) and consistent with the estimated hydration extent derived from the SV-wave velocities (Eimer et al., 2020).

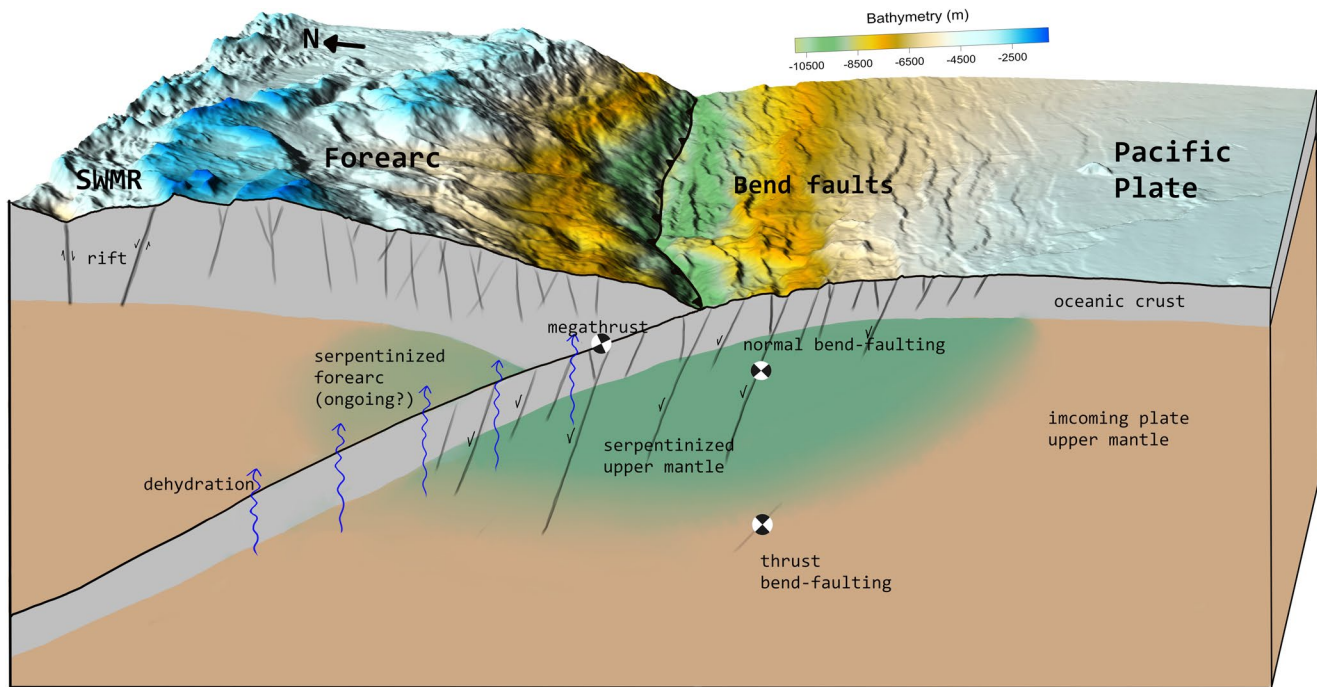


Figure 4. A conceptual model showing the serpentinized incoming plate due to the normal bend-faulting and the serpentinized forearc mantle due to slab dehydration in southern Mariana.

In southern Mariana, the distribution of the incoming plate seismicity located with OBSs also shows coherence with the hydration zone, although their focal mechanisms are unknown and location uncertainties are relatively large in the incoming plate. Numerous earthquakes have been found at the outer-rise and trench slope region within the incoming plate in southern Mariana (Zhu et al., 2019). Incoming plate seismicity occurs up to about 100 km seaward from the trench, and the number of earthquakes increases toward the trench (Figure 1c). Most of the incoming plate earthquakes that occurred within the calculated extensional yield zone were expected to be normal faulting, based on the calculated models matching the bathymetry of the bending plate. The SV-wave seismic velocity contour of 4.1 km/s matches well with the estimated maximum depth of extensional faulting (Figure 1c). Such a coherence indicates the depth extent of extensional failures is closely related to the hydrous low velocities zone within the oceanic plate, which corresponds to the region of a partial serpentinization zone in the mantle (Figure 4). The large maximum depth indicated by earthquakes of the extensional yield zone may also suggest large water input in the MSZ.

5.3. “Less” Hydrated Forearc Mantle

The velocity reduction of the forearc mantle at the southern Mariana (Figure 3a) is not as large as that in central Mariana (Cai et al., 2018), indicating the forearc mantle of southern Mariana may have a lower serpentinization degree compared with central Mariana. This is consistent with the existence of many serpentine seamounts and mud volcanos in central Mariana (Fryer et al., 1999), and few or no such features in southern Mariana. The difference in serpentinization degrees between southern and central Mariana probably reflects the different geological processes and the development of the forearc mantle in the two regions. The southern forearc is regarded as a more tectonic active region due to a combined effect of back-arc opening of the Mariana Trough and the presence of a short Pacific Plate slab which is rolling back rapidly (Okumura et al., 2016). The continuous extension of the southernmost Mariana forearc may inhibit fluid focusing, serpentinization of the forearc mantle, and seamount growth (Ribeiro et al., 2020). Therefore, the southern forearc is not associated with a discernible serpentinite mud volcano, except several samples of serpentinized peridotites from two dredge sites, suggesting a hydrous mantle beneath the forearc in this region (Ohara et al., 2012).

6. Conclusions

The first SV-wave velocity model of the southernmost Mariana Trench is derived using Rayleigh wave tomographic methods in this study. The incoming Pacific Plate is marked by low shear-wave velocities (3.6–4.1 km/s) within the upper ~25 km of the mantle near the trench, likely related to the mantle serpentinization percentage of ~19–41 vol% (i.e., ~1.9–4.3 wt%), indicating large water input in the southern Mariana Trench. The imaged low-velocity zone also matches well with the calculated extensional yield zone and the distribution of the incoming plate seismicity. The velocity reduction of the forearc mantle in southernmost Mariana is not as large as that of the central Mariana, possibly indicating a lower forearc serpentinization degree due to active extension of the southernmost Mariana forearc.

Data Availability Statement

The calculated ambient noise cross-correlation data and raw teleseismic data are available online (<https://figshare.com/articles/dataset/southernMariana/14183123>).

Acknowledgments

Constructive comments from two anonymous reviewers help improve the manuscript. We thank Zongshan Li and Jiangyang Zhang for their helpful discussions. Chen Cai shared his velocity model in the central Mariana and provided constructive help. Thanks to the science parties and crew members of the R/V Shiyan 3 and Tansuo 1 for deployment and recovery of the OBS instruments. This study is supported by the Hong Kong Research Grant Council Grants (No. 14313816), National Natural Science Foundation of China (Nos. 91858207, 41890813, and 91628301), Chinese Academy of Sciences (Nos. Y4SL021001, QYZDY-SSW-DQC005, 133244KYSB20180029, and COMS2019Q10), and National Key R&D Program of China (Nos. 2018YFC0309800, 2018YFC0310105, and 2018YFC0308003), Southern Marine Science and Engineering Guangdong Laboratory (Guangzhou) (No. GML2019ZD0205), Faculty of Science at CUHK.

References

- Arculus, R., Ishizuka, O., Bogus, K., Gurnis, M., Hickey-Vargas, R., Aljehdali, M. H., et al. (2015). A record of spontaneous subduction initiation in the Izu–Bonin–Mariana arc. *Nature Geosciences*, 8, 728–733. <https://doi.org/10.1038/ngeo2515>
- Barmin, M. P., Ritzwoller, M. H., & Levshin, A. L. (2001). A fast and reliable method for surface wave tomography. *Pure and Applied Geophysics*, 158, 1351–1375. <https://doi.org/10.1007/pl00001225>
- Bensen, G. D., Ritzwoller, M. H., Barmin, M. P., Levshin, A. L., Lin, F., Moschetti, M. P., et al. (2007). Processing seismic ambient noise data to obtain reliable broad-band surface wave dispersion measurements. *Geophysical Journal International*, 169(3), 1239–1260. <https://doi.org/10.1111/j.1365-246x.2007.03374.x>
- Cai, C., Wiens, D. A., Shen, W., & Eimer, M. (2018). Water input into the Mariana Subduction Zone estimated from ocean-bottom seismic data. *Nature*, 563, 389–392. <https://doi.org/10.1038/s41586-018-0655-4>
- Chapple, W. M., & Forsyth, D. W. (1979). Earthquakes and bending plates at trenches. *Journal of Geophysical Research*, 84, 6729–6749. <https://doi.org/10.1029/jb084ib12p06729>
- Eimer, M., Wiens, D. A., Cai, C., Lizarralde, D., & Jaspersen, H. (2020). Seismicity of the incoming plate and forearc near the Mariana Trench recorded by ocean bottom seismographs. *Geochemistry, Geophysics, Geosystems*, 21, e2020GC008953. <https://doi.org/10.1029/2020gc008953>
- Emry, E. L., Wiens, D. A., & Daniel, G. C. (2014). Faulting within the Pacific plate at the Mariana Trench: Implications for plate interface coupling and subduction of hydrous minerals. *Journal of Geophysical Research: Solid Earth*, 119(4), 3076–3095. <https://doi.org/10.1002/2013jb010718>
- Feng, L., & Ritzwoller, M. H. (2019). A 3-D shear velocity model of the crust and uppermost mantle beneath Alaska including apparent radial anisotropy. *Journal of Geophysical Research: Solid Earth*, 124, 19468–10497. <https://doi.org/10.1029/2019jb018122>
- Fryer, P. (1996). Evolution of the Mariana convergent plate margin system. *Reviews of Geophysics*, 34(1), 89–125. <https://doi.org/10.1029/95rg03476>
- Fryer, P., Wheat, C. G., & Mottl, M. J. (1999). Mariana blueschist mud volcanism: Implications for conditions within the subduction zone. *Geology*, 27(2), 103–106. [https://doi.org/10.1130/0091-7613\(1999\)027<0103:mbmvif>2.3.co;2](https://doi.org/10.1130/0091-7613(1999)027<0103:mbmvif>2.3.co;2)
- Fujie, G., Kodaira, S., Kaiho, Y., Yamamoto, Y., Takahashi, T., Miura, S., & Yamada, T. (2018). Controlling factor of incoming plate hydration at the north-western Pacific margin. *Nature Communications*, 9, 3844. <https://doi.org/10.1038/s41467-018-06320-z>
- Fujie, G., Kodaira, S., Sato, T., & Takahashi, T. (2016). Along-trench variations in the seismic structure of the incoming Pacific plate at the outer rise of the northern Japan Trench. *Geophysical Research Letters*, 43, 666–673. <https://doi.org/10.1002/2015gl067363>
- Grove, T. L., Till, C. B., Lev, E., Chatterjee, N., & Medard, E. (2009). Kinematic variables and water transport control the formation and location of arc volcanoes. *Nature*, 459, 694–697. <https://doi.org/10.1038/nature08044>
- Hayes, G. P., Moore, G. L., Portner, D. E., Hearne, M., Flamme, H., Furtney, M., & Smoczyk, G. M. (2018). Slab2, a comprehensive subduction zone geometry model. *Science*, 362, 58–61. <https://doi.org/10.1126/science.aat4723>
- Hirschmann, M. M. (2006). Water, melting, and the deep Earth H₂O cycle. *Annual Review of Earth and Planetary Sciences*, 34, 629–653. <https://doi.org/10.1146/annurev.earth.34.031405.125211>
- Hirth, G., & Kohlstedt, D. L. (1996). Water in the oceanic upper mantle: Implications for rheology, melt extraction and the evolution of the lithosphere. *Earth and Planetary Science Letters*, 144(1–2), 93–108. [https://doi.org/10.1016/0012-821x\(96\)00154-9](https://doi.org/10.1016/0012-821x(96)00154-9)
- Hyndman, R. D., & Peacock, S. M. (2003). Serpentinization of the forearc mantle. *Earth and Planetary Science Letters*, 212, 417–432. [https://doi.org/10.1016/s0012-821x\(03\)00263-2](https://doi.org/10.1016/s0012-821x(03)00263-2)
- Ji, S., Li, A., Wang, Q., Long, C., Wang, H., Marcotte, D., & Salisbury, M. (2013). Seismic velocities, anisotropy, and shear-wave splitting of antigorite serpentinites and tectonic implications for subduction zones. *Journal of Geophysical Research*, 118, 1015–1037. <https://doi.org/10.1002/jgrb.50110>
- Jin, G., & Gaherty, J. B. (2015). Surface wave phase-velocity tomography based on multichannel cross-correlation. *Geophysical Journal International*, 201, 1383–1398. <https://doi.org/10.1093/gji/ggv079>
- Kato, T., Beavan, J., Matsushima, T., Kotake, Y., Camacho, J. T., & Nakao, S. (2003). Geodetic evidence of back-arc spreading in the Mariana Trough. *Geophysical Research Letters*, 30(12), 1625. <https://doi.org/10.1029/2002gl016757>
- Kennett, B. L. N., & Engdahl, E. R. (1991). Travel times for global earthquake location and phase association. *Geophysical Journal International*, 105, 429–465. <https://doi.org/10.1111/j.1365-246x.1991.tb06724.x>
- Levshin, A. L., & Ritzwoller, M. H. (2001). Automated detection, extraction, and measurement of regional surface waves. *Pure and Applied Geophysics*, 158(8), 1531–1545. <https://doi.org/10.1007/pl00001233>

- Lin, F.-C., Moschetti, M. P., & Ritzwoller, M. H. (2008). Surface wave tomography of the western United States from ambient seismic noise: Rayleigh and Love wave phase velocity maps. *Geophysical Journal International*, *173*, 281–298. <https://doi.org/10.1111/j.1365-246x.2008.03720.x>
- Lin, F.-C., Ritzwoller, M. H., & Snieder, R. (2009). Eikonal tomography: Surface wave tomography by phase front tracking across a regional broad-band seismic array. *Geophysical Journal International*, *177*, 1091–1110. <https://doi.org/10.1111/j.1365-246x.2009.04105.x>
- Martinez, F., Stern, R.J., Kelley, K. A., Ohara, Y., Sleeper, J. D., Ribeiro, J. M., & Brounce, M. (2018). Diffuse extension of the Southern Mariana margin. *Journal of Geophysical Research: Solid Earth*, *123*(1), 892–916. <https://doi.org/10.1002/2017jb014684>
- Ohara, Y., Reagan, M. K., Fujikura, K., Watanabe, H., Michibayashi, K., Ishii, T., et al. (2012). A serpentinite-hosted ecosystem in the Southern Mariana Forearc. *Proceedings of the National Academy of Sciences*, *109*, 2831–2835. <https://doi.org/10.1073/pnas.1112005109>
- Okumura, T., Ohara, Y., Stern, R.J., Yamanaka, T., Onishi, Y., Watanabe, H., et al. (2016). Brucite chimney formation and carbonate alteration at the Shinkai Seep Field, a serpentinite-hosted vent system in the southern Mariana forearc. *Geochemistry, Geophysics, Geosystems*, *17*, 3775–3796. <https://doi.org/10.1002/2016gc006449>
- Ranero, C. R., Phipps Morgan, J., McIntosh, K., & Reichert, C. (2003). Bending-related faulting and mantle serpentinization at the Middle America trench. *Nature*, *425*, 367–373. <https://doi.org/10.1038/nature01961>
- Ribeiro, J. M., Ishizuka, O., Lee, C.-T. A., & Girard, G. (2020). Evolution and maturation of the nascent Mariana arc. *Earth and Planetary Science Letters*, *530*, 115912. <https://doi.org/10.1016/j.epsl.2019.115912>
- Ritzwoller, M. H., & Levshin, A. L. (1998). Surface wave tomography of Eurasia: Group velocities. *Journal of Geophysical Research: Solid Earth*, *103*, 4839–4878. <https://doi.org/10.1029/97jb02622>
- Shen, W., & Ritzwoller, M. H. (2016). Crustal and uppermost mantle structure beneath the United States. *Journal of Geophysical Research: Solid Earth*, *121*, 4306–4342. <https://doi.org/10.1002/2016jb012887>
- Shen, W., Ritzwoller, M. H., Kang, D., Kim, Y., Lin, F., Ning, J., et al. (2016). A seismic reference model for the crust and uppermost mantle beneath China from surface wave dispersion. *Geophysical Journal International*, *206*(2), 954–979. <https://doi.org/10.1093/gji/ggw175>
- Shen, W., Ritzwoller, M. H., Schulte-Pelkum, V., & Lin, F.-C. (2013). Joint inversion of surface wave dispersion and receiver functions: A Bayesian Monte-Carlo approach. *Geophysical Journal International*, *192*, 807–836. <https://doi.org/10.1093/gji/ggs050>
- Shillington, D., Bécel, A., Nedimović, M., Kuehn, K., Webb, S., Abers, G. A., et al. (2015). Link between plate fabric, hydration and subduction zone seismicity in Alaska. *Nature Geoscience*, *8*, 961–964. <https://doi.org/10.1038/ngeo2586>
- Stern, R. J., Fouch, M. J., & Klempere, S. L. (2003). An Overview of the Izu-Bonin-Mariana Subduction Factory. In *Inside the Subduction Factory* (Vol. 138, pp. 175–222). Geophysical Monograph, American Geophysical Union. <https://doi.org/10.1029/138gm10>
- Stern, R. J., Tamura, Y., Masuda, H., Fryer, P., Martinez, F., Ishizuka, O., & Bloomer, S. H. (2013). How the Mariana Volcanic Arc ends in the south. *Island Arc*, *22*, 133–148. <https://doi.org/10.1111/iar.12008>
- Tibi, R., Wiens, D. A., & Yuan, X. (2008). Seismic evidence for widespread serpentinized fore-arc mantle along the Mariana convergence margin. *Geophysical Research Letters*, *35*(13), L13303. <https://doi.org/10.1029/2008gl034163>
- Van Keken, P. E., Hacker, B. R., Syracuse, E. M., & Abers, G. A. (2011). Subduction factory: 4. Depth-dependent flux of H₂O from subducting slabs worldwide. *Journal of Geophysical Research*, *116*, B01401. <https://doi.org/10.1029/2010jb007922>
- Wan, K., Lin, J., Xia, S., Sun, J., Xu, M., Yang, H., et al. (2019). Deep seismic structure across the southernmost Mariana trench: Implications for arc rifting and plate hydration. *Journal of Geophysical Research: Solid Earth*, *124*, 4710–4727. <https://doi.org/10.1029/2018jb017080>
- Zhang, F., Lin, J., & Zhan, W. (2014). Variations in oceanic plate bending along the Mariana trench. *Earth and Planetary Science Letters*, *401*, 206–214. <https://doi.org/10.1016/j.epsl.2014.05.032>
- Zhang, F., Lin, J., Zhou, Z., Yang, H., & Zhan, W. (2018). Intra- and intertrench variations in flexural bending of the Manila, Mariana and global trenches: Implications on plate weakening in controlling trench dynamics. *Geophysical Journal International*, *212*, 1429–1449. <https://doi.org/10.1093/gji/ggx488>
- Zhou, Z., & Lin, J. (2018). Elasto-plastic deformation and plate weakening due to normal faulting in the subducting plate along the Mariana Trench. *Tectonophysics*, *734–735*, 59–68. <https://doi.org/10.1016/j.tecto.2018.04.008>
- Zhou, Z., Lin, J., Behn, M. D., & Olive, J.-A. (2015). Mechanism for normal faulting in the subducting plate at the Mariana Trench. *Geophysical Research Letters*, *42*(11), 4309–4317. <https://doi.org/10.1002/2015gl063917>
- Zhu, G., Yang, H., Lin, J., & You, Q. (2020). Determining the orientation of ocean bottom seismometers on the seafloor and correcting for polarity flipping via polarization analysis and waveform modelling. *Seismological Research Letters*, *91*(2A), 814–825. <https://doi.org/10.1785/0220190239>
- Zhu, G., Yang, H., Lin, J., Zhou, Z., Xu, M., Sun, J., & Wan, K. (2019). Along-strike variation in slab geometry at the Southern Mariana Subduction Zone revealed by seismicity through ocean bottom seismic experiments. *Geophysical Journal International*, *218*, 2122–2135. <https://doi.org/10.1093/gji/ggz272>